

Air and surface temperature coupling in the convective atmospheric boundary layer

Anirban Garai, Jan Kleissl¹

Dept of Mechanical and Aerospace Engineering, University of California, San Diego

¹ *Corresponding author address:* Jan Kleissl, Department of Mechanical and Aerospace Engineering, University of California, San Diego, 9500 Gilman Drive, EBUII – 580, La Jolla, CA 92093-0411

e-mail: jkleissl@ucsd.edu

Abstract:

In the convective boundary layer, besides shear, buoyancy is the dominating mechanism for turbulence production near the surface. Coherent structures were detected through their thermal signature on an artificial turf surface using high frequency thermal infrared (TIR) imagery and surface layer turbulence measurements. The coherent structures cause surface temperature variations over tens of seconds and spatial scales of tens to a few hundred meters. Air temperature at 1.5 m was correlated to ground temperature in a region of width of about 5 m extending upwind and downwind from the sensor. The coherent structures appear to be driven by mixed layer turbulence, since their speed is ~ 1.5 times greater than wind speed measured at 1.5 m above ground. Practical implications of turbulence-driven surface temperature variability for thermal remote sensing are also discussed.

Keywords: Convection, Surface Renewal, Surface Temperature, Thermal Infrared

1 Introduction

Buoyancy driven by solar heating of the earth's surface is one of the dominant mechanism driving turbulence in a convective boundary layer. Such turbulence is not random but is organized into structures, such as thermals and plumes. Plumes are coherent structures of rising warm air having diameters and depths on the order of the atmospheric surface layer (ASL, Kaimal and Businger 1970; Wilczak and Tillman 1980). Above the ASL these plumes become more diffuse and combine to form thermals which have larger length scales, of the order of the atmospheric boundary layer (Caughey and Palmer 1979; Young 1988; Deardorff and Willis 1985). Even though buoyancy is the dominant force to drive the plume, the ambient wind also modifies its structure. The plume advection velocity is close to the average wind speed over its depth. However, wind shear causes the plume to tilt by about 45° in the flow direction (Stull 1997).

Townsend (1958) performed an experiment on turbulent free convection over a heated horizontal surface in the laboratory and extended theoretical predictions to the atmospheric boundary layer. Temperature fluctuations, gradients, and rate of change of temperature all showed periodic activity, characterized by alternating large fluctuations and periods of quiescence. Liu and Businger (1975) proposed an analytical model for heat transfer during forced and free convection based on turbulent flow visualization. Following the studies of Kline et al. (1967) and Corino and Brodkey (1969) on turbulent structures in the near (smooth and rough) wall region Brutsaert (1975) assumed that the eddies responsible for plume-like structures are of the order Kolmogorov scale for smooth walls and roughness height for rough walls.

From the time series of velocity and temperature fluctuations and momentum and heat flux at a Kansas field site Kaimal and Businger (1970) proposed a two-dimensional model for the plumes and dust devils. Renno et al. (2004) found that dust devils can produce two to five times the average vertical turbulent flux of heat and dust. Using field experimental measurements at a flat site in northwestern Minnesota (Kaimal et al. 1976) and Colorado (Wilczak and Tillman 1980; Wilczak and Businger 1983) three dimensional structures driven by convection in the ASL and the 'energetics' of thermal structures over the entire boundary layer were examined.

Gao et al. (1989), Paw U et al. (1992), Braaten et al. (1993) and Raupach et al. (1996) studied coherent turbulent structures, known as surface renewal (SR) events, in different

canopies. In the SR process (Fig. 1a) a cold air parcel approaches the ground during a sweep. As it stays in contact with the ground heat is transferred from the ground to the parcel, until it has sufficient buoyant force. The heated air parcel then ascends during the ejection event. Thus the air temperature time series contains sawtooth or ramp like features (Fig. 1b). These ramp patterns were most clearly seen in the middle and upper portion of the canopy. Utilizing the characteristics of these coherent structures, Paw U et al. (1995), Snyder et al. (1996), Spano et al. (1997, 2000), Castellvi et al. (2002), Castellvi (2004) and Castellvi and Snyder (2009) proposed and validated the SR method to estimate surface sensible and latent heat fluxes given the statistics of high frequency air temperature measurements.

Atmospheric turbulence causes high frequency ground temperature fluctuations that cannot be explained by variability in solar irradiance alone. Paw U et al. (1992), Katul et al. (1998) and Renno et al. (2004) observed such surface temperature fluctuation of around 0.5 °C over 2.6 m high maize crops under unstable condition, greater than 2 °C over a 1 m high grass covered forest clearing and 2-4 °C over a desert area, respectively. The fluctuations were attributed to inactive eddy motions (Katul et al. 1998) and convective mixed layer processes (Renno et al. 2004). According to Townsend's hypothesis turbulent motion in the inner layer of boundary layer is composed of i) "active" part due to the shear near the surface, and ii) "inactive" part due to outer region turbulence. The evidence of inactive part of eddy motion can be studied from the near surface pressure fluctuation and lower wavenumber part spectra of longitudinal velocity (Katul et al. 1996). Vogt (2008) and Christen and Voogt (2009, 2010) visualized the spatial surface temperature field over a bare field and in a suburban street canyon using 1 Hz thermal infrared (TIR) imagery, respectively. Heat transport from urban lawns was qualitatively attributed to coherent structures and small scale turbulence. Balick et al. (2003) studied spatial variation of surface temperature from satellite imagery and modified the Brutsaert-Liu-Businger surface renewal approach to couple surface temperature with turbulent heat flux. From 1 Hz TIR data Kustas et al. (2002) studied the energy budget at a riparian corridor.

While turbulent coherent structures in the convective boundary layer are well-understood, their effect on the surface skin temperature is less studied. Our objective is to connect these different research areas by analyze the spatio-temporal structure of skin temperature fluctuations and their coupling to atmospheric turbulent coherent structures. Ultimately this research could lead to a more fundamental understanding of land-atmosphere

interaction and heat transfer at the earth's surface. In Sections 2, 3, and 4 we describe experimental method, results, and conclusions, respectively.

2 Experiment and Data Processing

2.1. Experimental set-up

The experiment was conducted over the 115x60 m Torrey Pines High School (TPHS) artificial turf football field (32°57' N, 117°23' W) on 1 May 2010 (Fig. 2). Surface albedo was measured as 0.06 (both for the visually lighter and darker 5 yard stripes) using a Kipp & Zonen CM6 thermopile albedometer. An additional experiment was conducted for stable conditions at the 285x150 m irrigated grass field (RIMAC) at University of California, San Diego (32°53' N, 117°14' W) on 10 August 2010. At RIMAC, the surface temperature variability consisted only of white noise, presumably because surface temperature variations were below the noise level of the TIR camera. This finding is consistent with the fact that coherent structures and air temperature variances are smaller in stable conditions. In the following we only report results from the TPHS study.

TIR images at TPHS were gathered using a FLIR A320 Thermacam operated at 1 Hz 15 m above ground level (a.g.l.). The TIR camera records longwave radiation from 8 to 14 μm wavelength in 240x320 pixels and converts them to surface temperature (T_g) assuming an emissivity of 0.95. The accuracy of T_g is 0.08 K. A coordinate system transformation and interpolation was performed to bird's eye view resulting footprints of 48x15 m with uniform resolution of 0.15x0.08 m (see an animation of the measurements in the video available from the last page of this document).

Global horizontal irradiance (GHI) was measured by a Licor 200SZ pyranometer. Turbulence data were measured using a Campbell Scientific Sonic-Anemometer-Thermometer (CSAT, measuring velocities u, v, w and sonic temperature T_s) and one fine wire thermocouple (measuring air temperature T_a) at 1.5 m a.g.l and at 10 Hz. For eddy-covariance flux measurements, we have used the thermocouple temperature instead of the sonic temperature, to nullify any effect of humidity on buoyancy. Since $|\langle w \rangle / M| < 0.0135$ (M is the mean horizontal wind speed and $\langle \cdot \rangle$ denotes time averaging), a coordinate system rotation was not necessary. Time-averaged (i.e. persistent) ground surface temperature ($\langle T_g \rangle_t$ as a function of x and y) variations of less than 10 K were observed and the tripod was placed within the camera footprint such that upwind $\langle T_g \rangle_t$ variations were small. Also, when $\langle T_g \rangle_t$ was subtracted from $T_g(x, y, t)$, visual inspection showed no effect of the spatial

heterogeneity on the evolution of $T_g'(x, y, t)$, where the prime denotes fluctuations about the temporal average.

2.2. Data Processing

The ogive test (Foken et al. 2006) revealed that a 5-min averaging period is sufficient for estimating the momentum and heat flux from the eddy covariance method. To ensure that the resulting time series are not affected by changes in meteorological conditions, fluctuations of wind speeds, temperature and ground temperature were calculated by removing the 5 min trends from the data

$$X'(t) = X(t) - (\langle X \rangle_{5min} + a_{X,5min}t), \quad (1)$$

where $a_{X,5min}$ is the linear time dependence coefficient of parameter X . For comparing 10 Hz turbulence data with 1 Hz T_g' data, we used a box filter of size 1-sec centered at the time stamp of T_g' . **The thermocouple air temperature was used to calculate the kinematic vertical**

turbulent flux of sensible heat $\langle w'T_a' \rangle$ since the sonic temperature is affected by humidity.

The heat flux footprint was estimated using the model proposed by Hsieh et al. (2000) in the streamwise direction. A cross-stream width of 3 m was assumed (see Fig. 5 later), which encompasses the region for which the footprint function is greater than 70% of its maximum for the conditions analyzed in Section 3. Then the weighted average of T_g' over the flux footprint was computed.

3 Results

Clear skies with south-westerly winds prevailed at TPHS (Fig. 3). The sensible heat flux was 200 to 400 W m⁻², $\langle T_g \rangle$ was 45-55 °C, horizontal wind speed was 1.5 to 3 m s⁻¹, and $\langle T_a \rangle$ was about 18 °C. Nearly constant Obukhov length ($L = -5.66$ m) and less wind direction variability (standard deviation of the wind direction less than 20°, not shown) motivated the selection of the period 1130-1200 PST for further analysis. During this time period, the friction velocity u_* was 0.26 m s⁻¹ and non-dimensional shear ($\frac{dM}{dz} \frac{z}{u_*}$) was 1.65. With the camera facing west at a beam angle of 18.8° from horizontal, solar noon at 1146 PST, and solar zenith angles of 18.1° or less, during this time period the grass blade shadows are small and their motion will have a small effect on changes in measured surface temperature. Assuming typical inversion height (z_i) about 500 m for the sea-breeze

meteorology in coastal California, convective velocity scale w_* , temperature scale T_* , time scale t_* , and flux Richardson number Ri were 1.62 m s^{-1} , 0.98 K , 309 s and -0.46 respectively.

The statistics of velocity and temperature fluctuations (standard deviation σ , skewness, kurtosis) are reported in Table 1. Fig. 4a-c depicts a typical 5-min time series of ground and air temperature, heat flux and (u', w') velocity. Ejection events (updrafts with positive w') occur less frequently but are associated with large heat fluxes than sweep events (downdrafts with negative w'). To study the lower frequency evolution of the temperature fluctuations we used wavelet analysis (Hudgins et al., 1993). For a time series, f , its wavelet function, W_f can be calculated by $W_f(s, \tau) = \int f(t)\psi_s(t - \tau)dt$ where s , τ , ψ_s are scale, time and mother wavelet function respectively. Thus wavelet analysis not only gives the spectral measure of variance, but also the time instant when it appears. We can use wavelets to detect when a surface renewal event is occurring and analyze wind speeds and temperatures during the event. In this study we will use Morlet as a mother wavelet.

Figure 4d-e shows the wavelet scalogram of the air and ground temperature fluctuation. There is a similarity between the T_a' and T_g' scalogram for scales of 60-sec and longer and the T_g' time series lags T_a' by about 20-sec. Consistent with the time series plot of T_g' and T_a' (Fig. 4a) and energy spectra (not shown), smaller scale T_a' fluctuations ($< 20 \text{ sec}$) have more energy than T_g' . This is due to the fact that the ground has a larger thermal mass than air and also due to the spatial averaging over the footprint. Consequently, the ground temperature signature of small eddies fall below the 0.08 K noise level of the TIR camera. The 1 Hz TIR data acquisition frequency (the highest possible with this TIR camera model) was sufficient to resolve the majority of T_g' fluctuations. The large scale fluctuations (scale $> 60 \text{ s}$) are correlated but out of phase: T_g' lags T_a' .

One would expect a correlation between T_a' and T_g' within the footprint of the CSAT (as seen in Fig. 4a). The temperature of an air parcel is due to its upwind ground footprint. When the ground becomes hot, the air will become hot and vice versa. Thus, the correlation between them should be maximum when the T_a' time series is lagged by the time it takes for air parcels to be advected from the footprint. Now as air moves downstream, it will affect the downstream ground temperature causing high correlation with positive lag. Fig. 5 shows the maximum correlation and corresponding lag between T_g' and T_a' , where a negative lag means

that T_g' preceded T_a' . The maximum correlation region aligns with the mean wind direction. Both the upstream and downstream region show high correlation in a region that extends up to 5 to 10 m in the streamwise direction, with negative lag upstream and positive lag downstream. While this is an expected result, this is the first time that this could be shown explicitly with spatial surface temperature data.

Figure 6 shows only the upstream correlation between T_g' and T_a' . The air temperature measurements are conducted at the coordinate origin (0-sec lag and 0 m distance). Upwind (negative distance) the lag with maximum correlation becomes negative. Consequently, this graph is a 2-dimensional depiction of correlation value (Fig. 5a) and lag (Fig. 5b) along a line upwind of the T_a' measurements. The slope of the line of maximum correlation indicates the velocity of the coherent structures. From the horizontal and vertical separation between a ground pixel and the T_a' sensor, the horizontal advection and vertical dispersion velocity of the coherent structures can be estimated, respectively. The estimated horizontal velocity is 3.30 m s^{-1} , which is greater than the mean wind speed at 1.5 m a.g.l. and the vertical velocity is 0.48 m s^{-1} , which is close to standard deviation of w (Table 1). The upwind maximum correlation region also is qualitatively consistent with the flux footprint function of Hsieh et al. (2000).

We now take further advantage of the spatial information provided by TIR camera to explore the manifestation of a renewal event. A sequence of snapshots of $T_g'(x, y)$ during a renewal event is shown in the upper panel of Fig. 7 for 114924-115054 PST (from 144 to 234 sec in Fig. 4). Initially T_g' is negative over the footprint (Fig. 7a) which can be attributed to a sweep event, when cold air comes in contact with ground (A in Fig. 1). Shortly thereafter, several small hot spots appear (Fig. 7b). These hot spots grow, combine, and are advected by the wind (B in Fig. 1). At the subsequent time T_g' in the entire image becomes positive (Fig. 7c) initiating an ejection event (C in Fig. 1). As the heated air rises from the ground due to its buoyancy, the ground starts to cool (Fig. 7d, D in Fig. 1) again.

To study these spatial structures we employ Principal Orthogonal Decomposition (POD, Pope, 2003). Large structures are reconstructed using the ten most energetic POD modes and small structures are constructed using the residual nodes (Fig. 7 middle and lower panels). We caution that since the size of the structures exceeds the size of the TIR camera image, the structures depicted here are not the largest structures. When the ground is either hot or cold (Figs. 7a,c), i.e. during sweep and ejection, the large structures are larger

compared to the time when ground is heating up or cooling down (Figs. 7b,d). Following the model of coherent eddies by Williams and Hacker (1992) and Vogt (2008), hot or cold ground (Figs. 7a,c) can be attributed to a transition between two roll vortices near the ground leading to large updrafts or downdrafts. The ground heating up or cooling down (Figs. 7b,d) can be attributed to a roll vortex being centered over the site leading to sweeping away of small eddies. On the other hand the residual small structures do not depend on the phase of the renewal event. Also the orientation of the large structures is more aligned with the wind direction compared to the residual small structures (Fig. 8).

Our analysis has shown that the dimensions of the surface temperature scales are larger than the TIR camera image (Figs. 7a,c) and their temporal scale is several advection time scales through the image (Fig. 4). Ideally the TIR camera footprint should be greater than the large scales, but even with our wide-angle lens this would require flying the camera on a stabilized balloon at several 100 m in altitude. To illustrate the spatio-temporal evolution of the structures, we draw a line through the image in streamwise direction and plot the time evolution of T_g' along this line for 1147-1152 PST in Fig. 9a. Most large events indeed last tens of seconds and are larger than 20 m in scale. Based on Fig. 9a, but considering all lines aligned in the streamwise direction, Fig. 9b provides the mean of the correlation statistics across space and time. The advective nature of the structures can be seen from the upward slope of the hot and cold 'stripes' of T_g' in Fig. 9a and the downward slope of the spatio-temporal correlation profile in Fig. 9b. The estimated horizontal velocity from the slope of spatio-temporal correlation profile for the structures is 3.18 m s^{-1} , which is also close to the estimated horizontal velocity from the ground-air correlation (Fig. 6). Also the high correlation region in Fig. 9b indicates both the temporal and spatial extent of a structure in the downwind direction.

4 Conclusions

In this proof-of-concept study we evaluate the ground and air temperature interaction for the convective atmospheric boundary layer using TIR imagery. With only data from one day presented, the analysis is not exhaustive and more extensive studies on the topic are needed, but practical issues (since the thermal camera is not waterproof and expensive it cannot be left unattended) and lack of funding make long-term studies difficult. Most existing

eddy covariance sites are not suitable to conduct the experiment since short vegetation is required. In the absence of vegetation (e.g. over a parking lot), the thermal admittance is too small and T_g' cannot be detected (not shown). If the vegetation is too high, 'honamis' or ocean-wave-like motion of crops will occur and the resulting shading and varying solar incidence angle pattern complicate the analysis (Finnigan, 2010). So, ideal site for this sort of experiment is a dry, flat surface (smaller roughness) with small vegetation and a high viewpoint for camera. Our site fulfilled all criteria except for large scale homogeneity. But, since the wind speed is low on the experiment day, the effect of shredded eddies by surrounding building is minimal. While other researchers have examined T_g variability, our study is the first to provide a thorough quantitative spatial analysis of surface-atmosphere exchange using TIR imagery.

The speed of the coherent structures was 1.5 times the wind speed at 1.5 m a.g.l. and consistent with a velocity at 6.5 m a.g.l. (estimated from the stability corrected log-profile). Christen and Voogt (2010) reported the speed of these coherent structures to be twice the wind speed at ~ 0.5 m a.g.l. This difference in ratio between the speed of the coherent structure and wind may be due to the fact Christen and Voogt (2010) gathered their measurement closer to the surface and inside a street canyon, compared to our open field. Katul et al. (1998) found T_g fluctuations are driven by the inactive eddy motion, which scaled as mixed layer turbulence. Our wavelet analysis showed that only large coherent structures leave a T_g signature and these structures (time scale > 60 s) are responsible for the majority of the sensible heat flux. Also air temperature at 1.5 m a.g.l. was correlated to upwind and downwind T_g in a region of width of about 5 m (about 3 times the measurement height).

In a convective atmospheric boundary layer, mixed layer roll vortices are the large-scale eddies responsible for transport of momentum, heat and mass. While we can only observe the manifestations of atmospheric turbulence on surface temperature, we believe that the observed patterns are consistent with the following concepts. The downward flowing part of this mixed layer roll vortex will cause cold air to approach the ground during a sweep event. This cold air in contact with the warm ground will cause a large heat flux from ground to the air, causing large portions of the TIR imagery to cool. With time the air heats up, causing heating up of the ground. This phenomenon manifests itself by small hot patches. As the air and ground heat-up, the warm air will result in an updraft due to its buoyancy, which represents the thermal or upward flowing part of mixed layer roll vortices or 3-D cells. After

the updraft, the surrounding cold air will approach the ground and the cycle repeats. As these roll vortices or 3-D cells move with wind, our TIR images also reveal that the ground temperature structures also advect in wind direction with time. Thus turbulence in the unstable atmospheric boundary layer induces coherent patterns of T_g fluctuations that can be visualized through TIR imagery. Also, we did not find any sort of ground temperature coherent patterns in a separate experiment in a stable boundary layer.

We observed within-image temporally averaged standard deviations of 0.7 K, which is 0.7 times the convective temperature scale, T_* , consistent with the value measured for a high resolution satellite image by Balick et al. (2003). The temporal standard deviation of T_g (Table 1) is also comparable with the studies carried out by Katul et al. (1998) and Renno et al. (2004). T_g fluctuations driven by atmospheric turbulence have practical implications for remote sensing e.g. of land mine signatures or evapotranspiration (ET) for irrigation management. Hydrologic energy balance models (e.g. SEBAL by Bastiaansen et al., 1998a,b) derive the sensible heat flux (and ET) through the surface energy balance from spatial differences in surface and air temperature. The large coherent structures can introduce physical ‘noise’ in ET estimates especially if single-image satellite or aerial TIR imagery at high spatial resolution is used.

Acknowledgements: We would like to express our gratitude to Greg Snelling at RIMAC field of UCSD and Mr. Garry W. Thornton at Torrey Pines High School for providing access to their fields. Billy Hayes, Anders Nottrott, KhristinaRae Hernandez provided field assistance. We are indebted to Jamie Voogt (University of Western Ontario) for discussing the experimental strategy. This study was funded by NSF CAREER and NASA New Investigator Program awards.

References

- Balick, L. K. , C. A. Jeffery, and B. Henderson, 2003: Turbulence induced spatial variation of surface temperature in high resolution thermal IR satellite imagery. *Proc. SPIE*, **4879**, 221-230.
- Bastiaanssen W. G. M., M. Menenti, R. A. Feddes, and A. A. M. Holtslag, 1998a: A remote sensing surface energy balance algorithm for land (SEBAL) 1. Formulation. *J. Hydrol.*, **212-213**, 198-212.
- Bastiaanssen W. G. M., H. Pelgrum, J. Wang, Y. Ma, J. F. Moreno, G. J. Roerink, R. A. Roebeling, and T. van der Wal, 1998b: A remote sensing surface energy balance algorithm for land (SEBAL) 2. Validation. *J. Hydrol.*, **212-213**, 213-229.
- Braaten D. A., R. H. Shaw, and K. T. Paw U, 1993: Boundary-layer flow structures associated with particle reentrainment. *Boundary-Layer Meteorol.*, **65**, 255-272.
- Brutsaert W., 1975: A theory for local evaporation (or heat transfer) from rough and smooth surfaces at ground level. *Water Resour. Res.*, **11**, 543-550.
- Castellvi F., 2004: Combining surface renewal analysis and similarity theory: a new approach for estimating sensible heat flux. *Water Resour. Res.*, **40**, W05201.
- Castellvi F., P. J. Perez, and M. Ibanez, 2002: A method based on high-frequency temperature measurements to estimate the sensible heat flux avoiding the height dependence. *Water Resour. Res.*, **38**(6), 1084.
- Castellvi F., and R. L. Snyder, 2009: Combining the dissipation method and surface renewal analysis to estimate scalar fluxes from the time traces over rangeland grass near Ione (California). *Hydrol. Process.*, **23**, 842-857.
- Caughey S. J., and S. G. Palmer, 1979: Some aspects of turbulence structure through the depth of the convective boundary layer. *Quart. J. R. Meteorol. Soc.*, **105**, 811-827.
- Christen A., and J.A. Voogt, 2009: Linking atmospheric turbulence and surface temperature fluctuations in a street canyon. Paper no. A3-6. *The 7th International Conference on Urban Climate*, Yokohoma, Japan.

- Christen A., and J. A. Voogt, 2010: Inferring turbulent exchange process in an urban street canyon from high-frequency thermography. Paper no. J3A.3. *9th Symposium on the Urban Environment*, Keystone, Colorado, USA.
- Corino E. R., and R. S. Brodkey, 1969: A visual investigation of the wall region in turbulent flow. *J. Fluid Mech.*, **37**, 1-30.
- Deardorff J. W., and G. E. Willis, 1985: further results from a laboratory model of the convective planetary boundary layer. *Boundary-Layer Meteorol.*, **32**, 205-236.
- Finnigan J. J., 2010: Waving plants and turbulent eddies. *J. Fluid Mech.*, **652**, 1-4.
- Foken T., F. Wimmer, M. Mauder, C. Thomas, and C. Liebenthal, 2006: Some aspects of the energy balance closure problem. *Atmos. Chem. Phys.*, **6**, 4395-4402.
- Gao W., R. H. Shaw, and K. T. Paw U, 1989: Observation of organized structure in turbulent flow within and above a forest canopy. *Boundary-Layer Meteorol.*, **47**, 349-377.
- Hsieh C-I., G. G. Katul, and T. Chi, 2000: An approximate analytical model for footprint estimation of scalar fluxes in thermally stratified atmospheric flows. *Adv. Water Resour.*, **23**, 765-772.
- Hudgins L., C. A. Friehe, and M. E. Mayer, 1993: Wavelet transforms and atmospheric turbulence. *Phys. Rev. Lett.*, **71**(20), 3279-3282.
- Kaimal J. C., and J. A. Businger, 1970: Case studies of a convective plume and a dust devil. *J. Appl. Meteorol.*, **9**, 612-620.
- Kaimal J. C., J. C. Wyngard, D. A. Haugen, O. R. Cote, and Y. Izumi, 1976: Turbulence structure in the convective boundary layer. *J. Atmos. Sci.*, **33**, 2152-2169.
- Katul G. G., J. D. Albertson, C-I Hsieh, P. S. Conklin, J. T. Sigmon, M. B. Parlange, and K. R. Knoerr, 1996: The “inactive” eddy motion and the large scale turbulent pressure fluctuations in the dynamic sublayer. *J. Atmos. Sci.*, **53**, 2512-2524.
- Katul G. G., J. Schieldge, C-I Hsieh, and B. Vidakovic, 1998: Skin temperature perturbations induced by surface layer turbulence above a grass surface. *Water Resour. Res.*, **34**, 1265-1274.

- Kline S. J., W. C. Reynolds, F. A. Schraub, and P. W. Runstadler, 1967: The structure of turbulent boundary layers. *J. Fluid Mech.*, **30**, 741-773.
- Kustas W. P., J. H. Prueger, and L. E. Hipps, 2002: Impact of using different time-averaged inputs for estimating sensible heat flux of riparian vegetation using radiometric surface temperature. *J. Appl. Meteorol.*, **41**, 319-332.
- Liu W. T., and J. A. Businger, 1975: Temperature profile in the molecular sublayer near the interface of a fluid in turbulent motion. *Geophys. Res. Lett.*, **2**, 403-404.
- Paw U K. T., Y. Brunet, S. Collineau, R. H. Shaw, T. Maitani, J. Qiu, and L. Hipps, 1992: On coherent structures in turbulence above and within agricultural plant canopies. *Agric. For Meteorol.*, **61**, 55-68.
- Paw U K. T., J. Qiu, H-B. Su, T. Watanabe, and Y. Brunet, 1995: Surface renewal analysis: a new method to obtain scalar fluxes. *Agric. For Meteorol.*, **74**, 119-137.
- Pope S. B., 2003: *Turbulent Flows*. Cambridge University Press, New York, USA, 771 pp.
- Raupach M. R., J. J. Finnigan, and Y. Brunet, 1996: Coherent eddies and turbulence in vegetation canopies: the mixing-layer analogy. *Boundary-Layer Meteorol.*, **78**, 351-382.
- Renno N. O., V. J. Abreu, J. Koch, P. H. Smith, O. K. Hartogensis, H. A. R. De Bruin, D. Burose, G. T. Delory, W. M. Farrell, C. J. Watts, J. Garatuza, M. Parker, and A. Carswell, 2004: MATADOR 2002: A pilot experiment on convective plumes and dust devils. *J. Geophys. Res.*, **109**, E07001.
- Snyder R. L., D. Spano, and K. T. Paw U, 1996: Surface renewal analysis for sensible and latent heat flux density. *Boundary-Layer Meteorol.*, **77**, 249-266.
- Spano D., R. L. Snyder, P. Duce, and K. T. Paw U, 1997: Surface renewal analysis for sensible heat flux density using structure functions. *Agric. For Meteorol.*, **86**, 259-271.
- Spano D., R. L. Snyder, P. Duce, and K. T. Paw U, 2000: Estimating sensible and latent heat flux densities from grapevine canopies using surface renewal. *Agric. For Meteorol.*, **104**, 171-183.

- Stull R. B., 1997: *An introduction to boundary layer meteorology*. Kluwer Academic Publishers, USA, 666 pp.
- Townsend A. A., 1958: Temperature fluctuation over a heated horizontal surface. *Fluid Mech.*, **5**, 209-241.
- Vogt R., 2008: Visualisation of turbulent exchange using a thermal camera. Paper no. 8B.1. *18th Symposium on Boundary Layer and Turbulence*, Stockholm, Sweden.
- Wilczak J. M., and J. A. Businger, 1983: Thermally indirect motions in the convective atmospheric boundary layer. *J. Atmos. Sci.*, **40**, 343-358.
- Wilczak J. M., and J. E. Tillman, 1980: The three-dimensional structure of convection in the atmospheric surface layer. *J. Atmos. Sci.*, **37**, 2424-2443.
- Williams A. G. and J. M. Hacker, 1992: Interactions between coherent eddies in the lower convective boundary layer. *Boundary-Layer Meteorol.*, **64**, 55-74.
- Young G. S., 1988: Convection in the atmospheric boundary layer. *Earth Sci. Rev.*, **25**, 179-198.

Figure captions

Figure 1. a) Schematic of an idealized surface renewal process and b) resulting temperature trace of the air parcel (adapted from Paw U et al. 1995).

Figure 2. a) Field of view of the thermal IR camera images at Torrey Pines High School, San Diego (the white star represents the position of the tripod and the blue arrow shows the prevalent wind direction), b) Tripod with the meteorological and turbulence sensors (only data from the upper anemometer was analyzed).

Figure 3. Time series of the 5-min averaged meteorological conditions, a) air and ground temperature ($\langle T_a \rangle$, $\langle T_g \rangle$ averaged over the TIR image), b) wind speed (M), c) global horizontal irradiance (GHI) and sensible heat flux (H) and d) Obukhov length (L), for the experiment at TPHS on 01 May 2010. The section between two vertical dotted lines represents the relatively stationary period considered for further analysis.

Figure 4. Time series of a) air and ground temperature fluctuations (average over footprint), b) kinematic heat flux, c) u - w -velocity vector and scaled wavelet scalogram of d) air and e) ground temperature fluctuations for 1147-1152 PST.

Figure 5. Spatial dependence of (a) maximum correlation and (b) corresponding time lag [sec] between air and ground temperature for 1130-1200 PST. The black vertical bar marks the location of the tripod and the black arrow represents the mean wind direction. The white region in Fig. 5b indicates a ground-air temperature correlation of less than 0.2.

Figure 6. Correlation map between air temperature and upwind ground temperature at different distances (x axis) and time lags. The horizontal white line represents zero lag.

Figure 7. Snapshots of ground temperature fluctuation (K) (upper panel) at $\Delta t =$ a) 0 s, b) 10 s, c) 55 s and d) 90 s during a renewal event starting at 114924 PST. Spatial correlation map for large (middle panel) and residual small (lower panel) structures are obtained from Principal Orthogonal Decomposition. The TIR temperature map is shown in the transformed coordinate system based on the original image of Fig. 2b and the wind direction is from upper left (south-westerly).

Figure 8. Average from 1130-1200 PST of the spatial correlation (colorbar) map for a) large and c) residual small T_g' structures based on POD with streamwise and spanwise correlation for b) large and d) residual small structures. Solid and dashed lines represent the mean streamwise and spanwise wind directions, respectively.

Figure 9. a) Temporal evolution of T_g' along a line through the image oriented in the stream wise direction. b) Spatio-temporal correlation of T_g' at a point to points upstream in the streamwise direction at distances of 0 to 20 m for different time lags.

Figures and tables

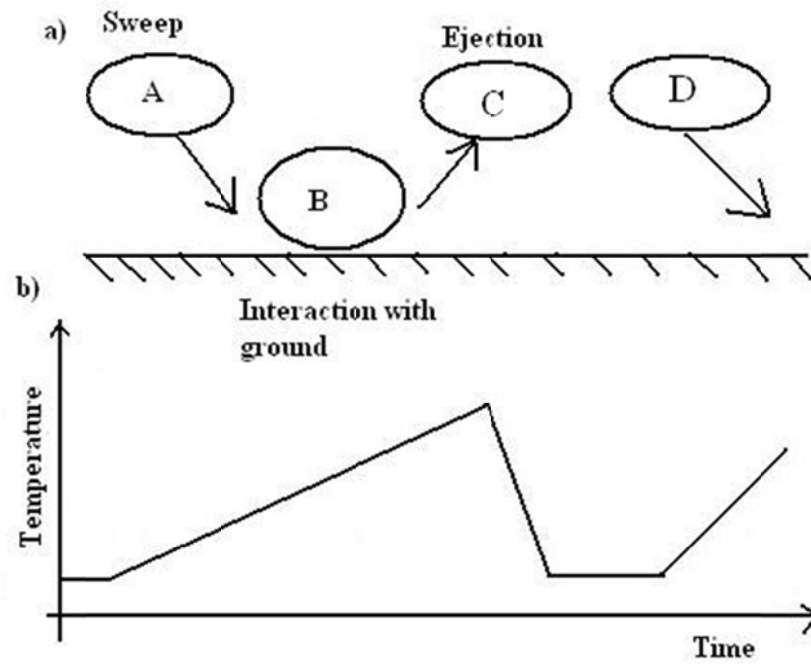


Figure 1. a) Schematic of an idealized surface renewal process and b) resulting temperature trace of the air parcel (adapted from Paw U et al. 1995).

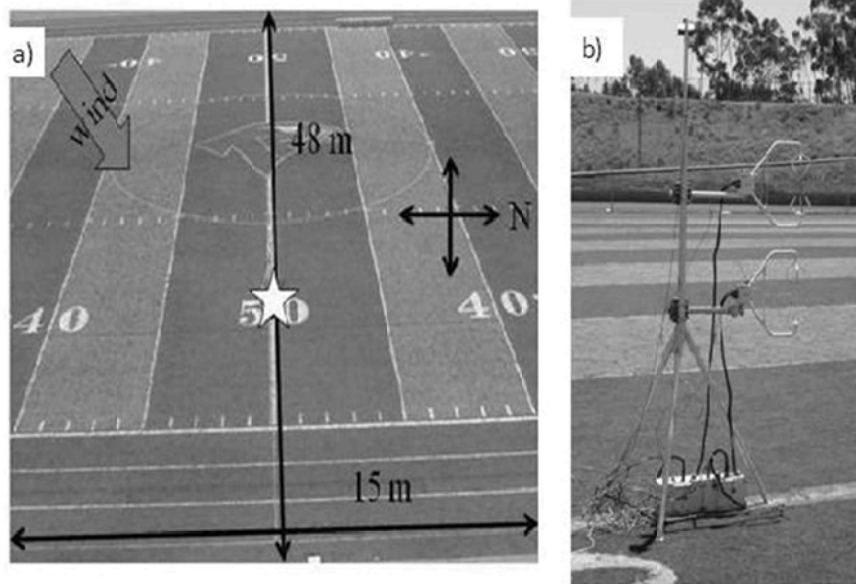


Figure 2. a) Field of view of the thermal IR camera images at Torrey Pines High School, San Diego (the white star represents the position of the tripod and the blue arrow shows the prevalent wind direction), b) Tripod with the meteorological and turbulence sensors (only data from the upper anemometer was analyzed).

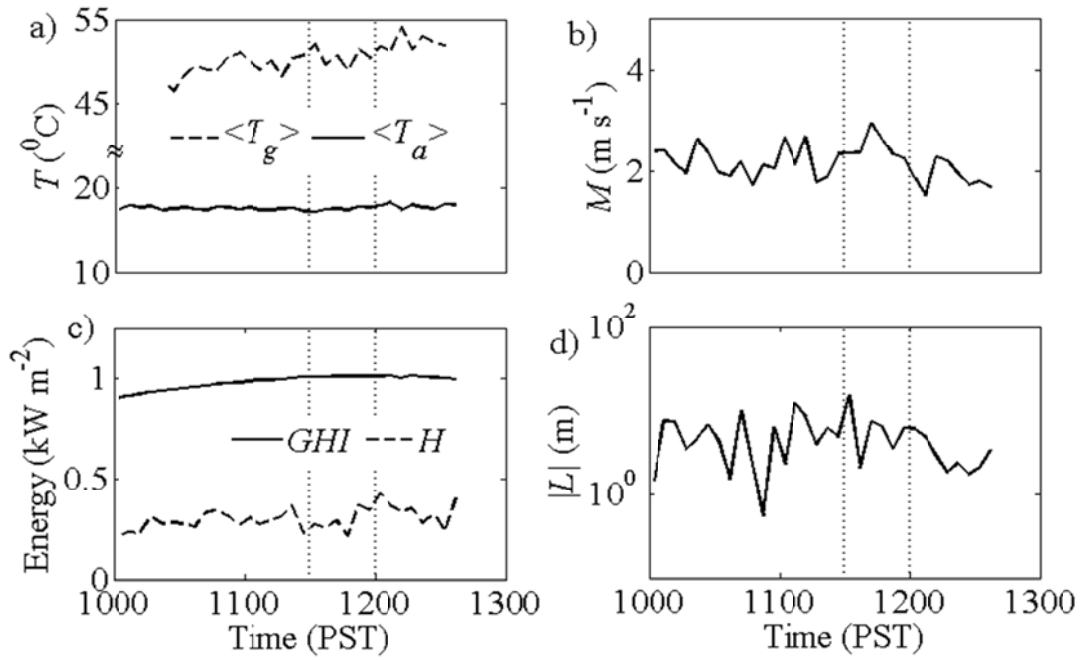


Figure 3. Time series of the 5-min averaged meteorological conditions, a) air and ground temperature ($\langle T_a \rangle$, $\langle T_g \rangle$ averaged over the TIR image), b) wind speed (M), c) global horizontal irradiance (GHI) and sensible heat flux (H) and d) Obukhov length (L), for the experiment at TPHS on 01 May 2010. The section between two vertical dotted lines represents the relatively stationary period considered for further analysis.

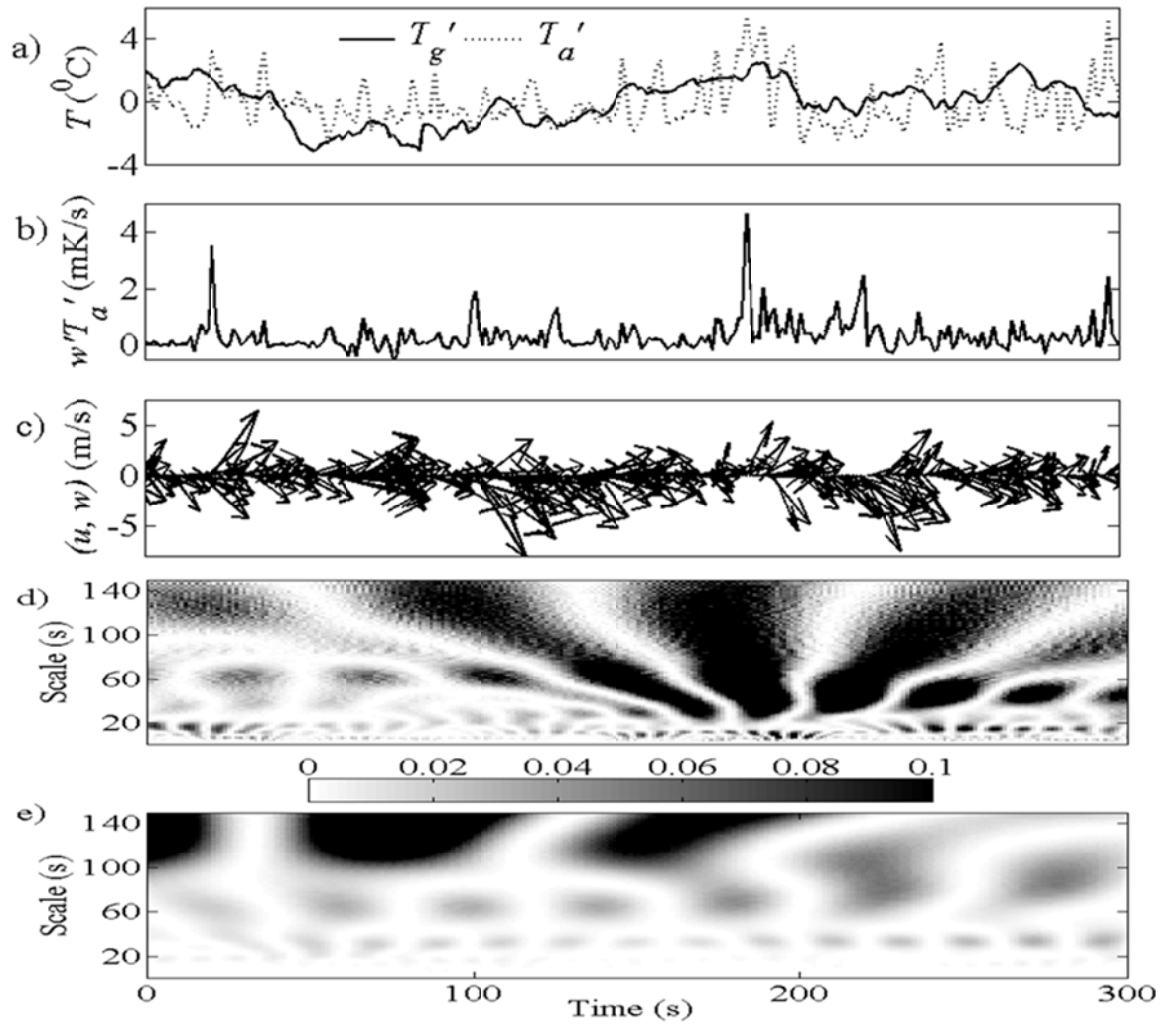


Figure 4. Time series of a) air and ground temperature fluctuations (average over footprint), b) kinematic heat flux, c) $u-w$ -velocity vector and scaled wavelet scalogram of d) air and e) ground temperature fluctuations for 1147-1152 PST.

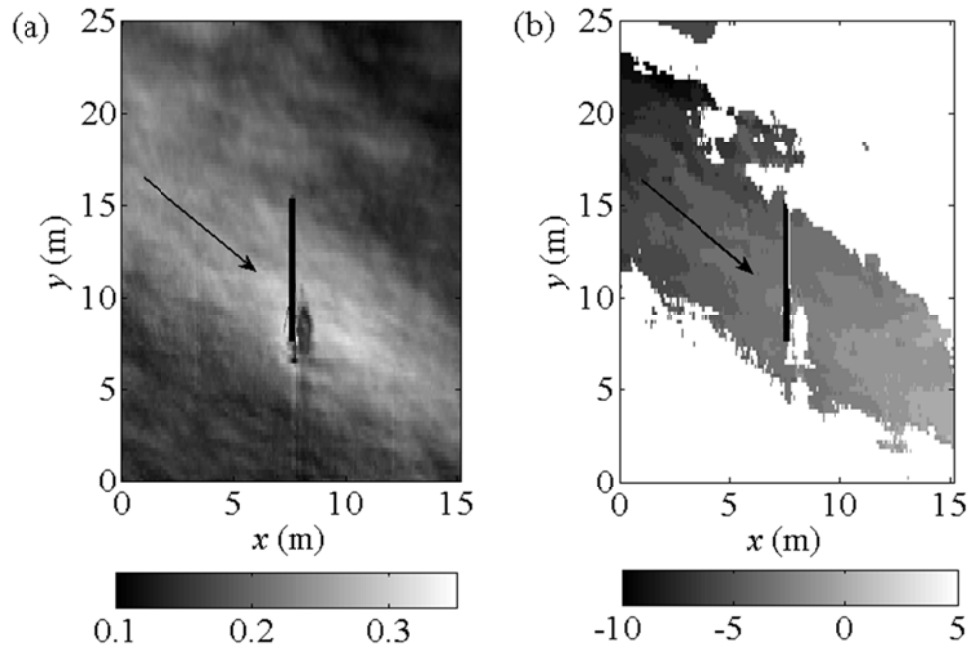


Figure 5. Spatial dependence of (a) maximum correlation and (b) corresponding time lag [sec] between air and ground temperature for 1130-1200 PST. The black vertical bar marks the location of the tripod and the black arrow represents the mean wind direction. The white region in Fig. 5b indicates a ground-air temperature correlation of less than 0.2.

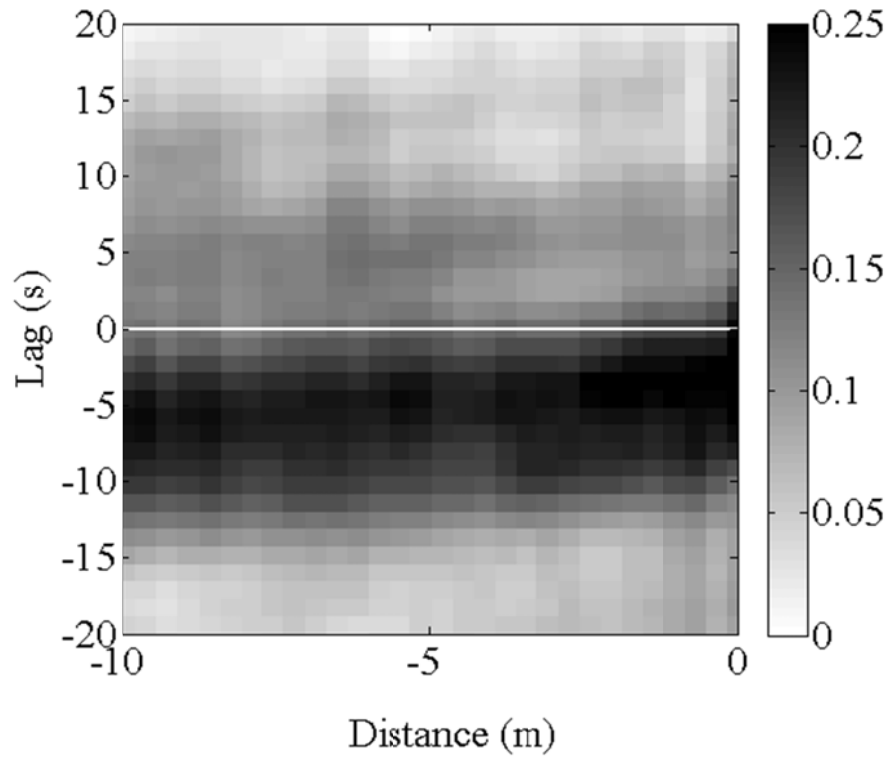


Figure 6. Correlation map between air temperature and upwind ground temperature at different distances (x axis) and time lags. The horizontal white line represents zero lag.

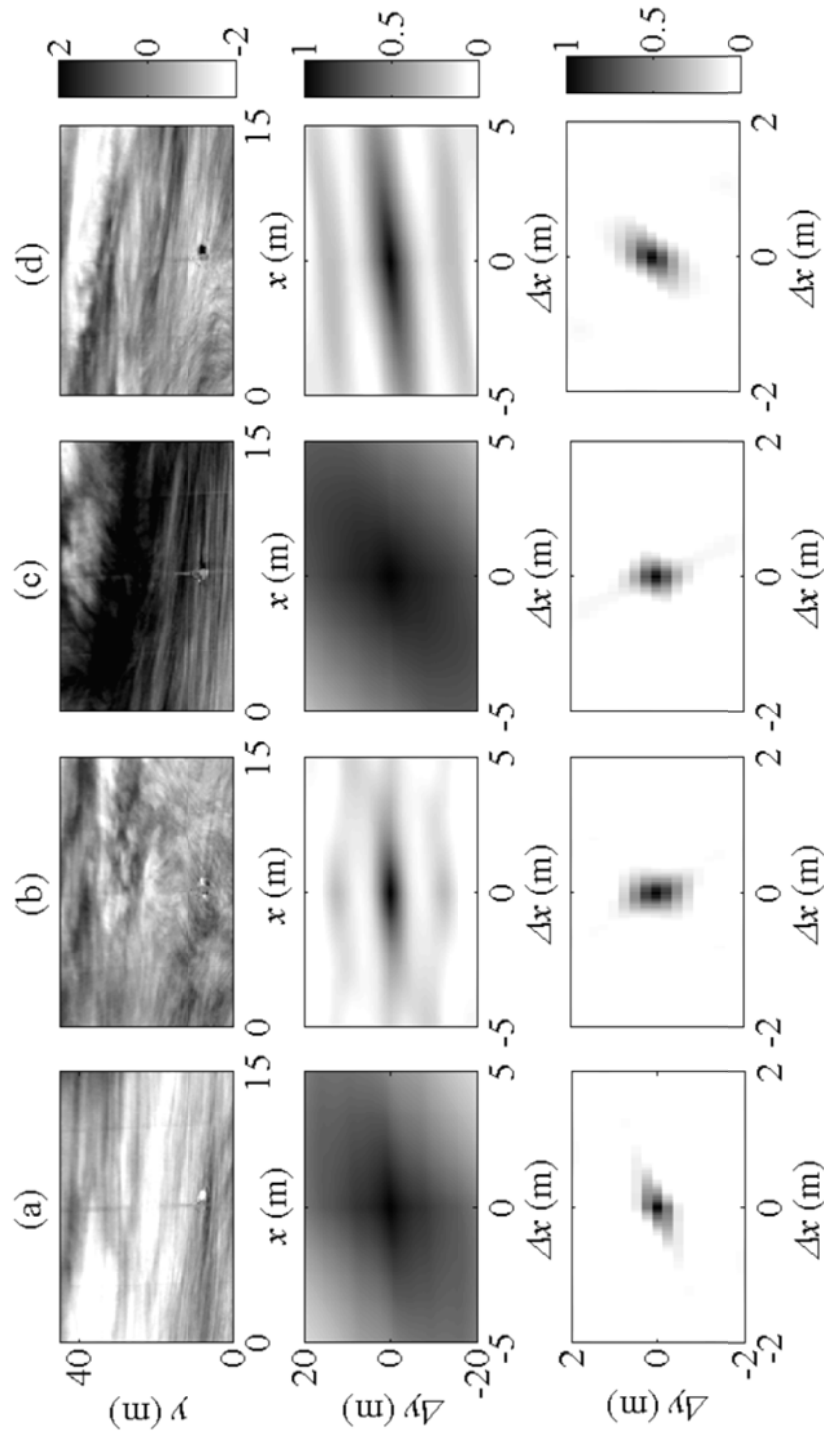


Figure 7. Snapshots of ground temperature fluctuation (K) (upper panel) at $\Delta t =$ a) 0 s, b) 10 s, c) 55 s and d) 90 s during a renewal event starting at 114924 PST. Spatial correlation map for large (middle panel) and residual small (lower panel) structures are obtained from Principal Orthogonal Decomposition. The TIR temperature map is shown in the transformed coordinate system based on the original image of Fig. 2b and the wind direction is from upper left (south-westerly).

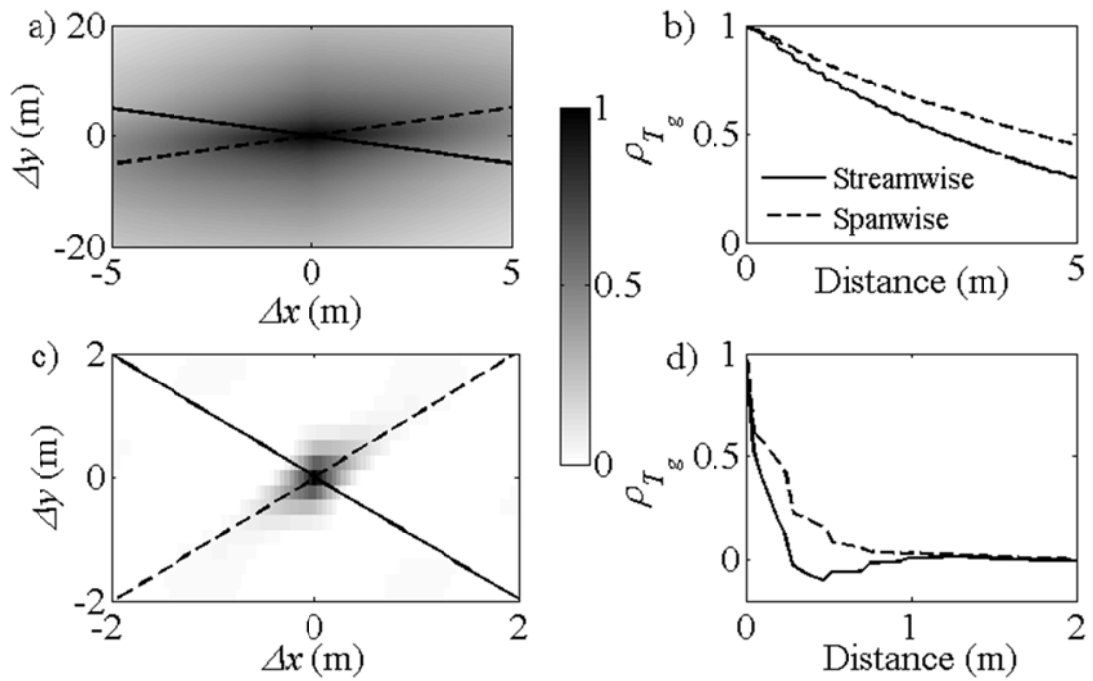


Figure 8. Average from 1130-1200 PST of the spatial correlation (colorbar) map for a) large and c) residual small T_g' structures based on POD with streamwise and spanwise correlation for b) large and d) residual small structures. Solid and dashed lines represent the mean streamwise and spanwise wind directions, respectively.

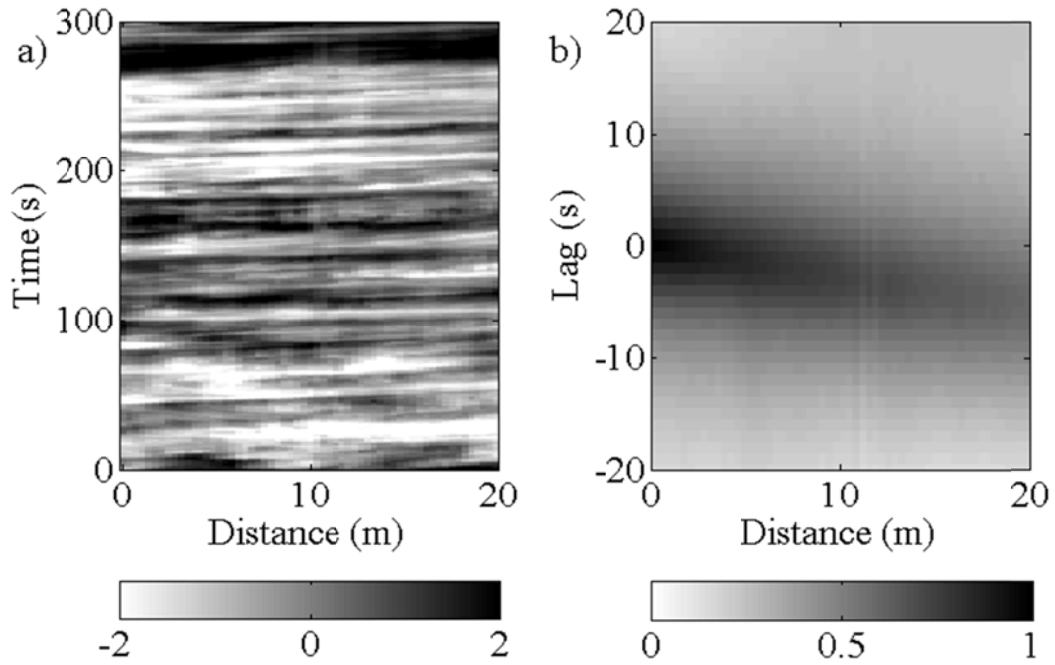


Figure 9. a) Temporal evolution of T_g' along a line through the image oriented in the stream wise direction. b) Spatio-temporal correlation of T_g' at a point to points upstream in the streamwise direction at distances of 0 to 20 m for different time lags.

Table 1. Standard deviation σ , skewness, and kurtosis of the velocity components, air temperature and ground temperature fluctuations during the 1130-1200 PST.

| | u | v | w | T_a | T_g |
|----------|------------------------|------------------------|------------------------|--------|--------|
| σ | 1.00 m s ⁻¹ | 1.20 m s ⁻¹ | 0.40 m s ⁻¹ | 1.60 K | 1.12 K |
| Skewness | 0.40 | 0.10 | -0.30 | 1.30 | -0.14 |
| Kurtosis | 3.25 | 3.01 | 4.34 | 4.80 | 3.48 |